Development and Repetitive-compensated PID Control of a Nanopositioning Stage with Large-stroke and Decoupling Property

Hui Tang, Jian Gao, Xin Chen, Kai-Ming Yu, Suet To, Yunbo He, Xun Chen, Zhaohe Zeng, Sifeng He, Chuangbin Chen, Yangmin Li, *Senior Member*, IEEE

***Abstract*—Piezoelectric actuator (PZT) driven nanopositioning stages, with large stroke and low cross-talk, are quite appealing for fulfilling the Through Silicon Via (TSV) lithography etching task. The motivation of this work is to combine the ability to enable the nanopositioning stage running in a manner of millimeter scale workspace and nanometer scale positioning accuracy. Two pairs of flexure-guided kinematic modules (FGKM) with high displacement amplification ratio (DAR) are adopted to construct a 4-PP(P is prismatic)XY nanopositioning stage. A new decoupling design is implemented to realize the decoupling behavior between the input actuators and output compliant limbs, respectively. Kinematics modeling including output compliance, input stiffness, displacement amplification ratio modeling, and workspace determination are carried out. After a series of mechanism dimension optimizations via Particle Swarm Optimization (PSO) algorithm, the performance of the optimized mechanism is analyzed and assessed by using the ANSYS Workbench. Then, a repetitive-compensated PID (RCPID) controller and a SISO closed-loop control strategy are designed. Finally, a series of experimental tests in terms of cross-talk test, frequency characteristic analysis, damping property analysis, dynamic hysteresis nonlinearity characterization, signal trajectory tracking, workspace determination, and Bode diagram plotting are carried out in details. It indicates that the workspace of fabricated prototype has reached to 1.035mm$\times$1.035mm, the cross-talk ratio is kept within 0.5%, and the closed-loop positioning accuracy is determined as 400nm.**

***Index Terms*—Nanopositioning stage, flexure, piezoelectric actuator, through silicon via, repetitive control.**

I. Introduction

In the "Post-Moore Era", miniaturization, multi-functionalization, and integration of electronic devices call for more integrated chip packaging technology. In the process of system-in-a-package(SiP) chip packaging, TSV lithography etching is the key process to guarantee high quality vertical connection on a substrate. During laser lithography, the interaction time between laser and materials is much shorter than the time for electrons to pass the energy to the lattice of the materials. Generally, the minimum diameter of TSV hole is only about 10μm, the depth width ratio is $>$10, as well as I/O density is $>$10e4/mm^2. Thus, how to simultaneously achieve high speed, high accuracy, and large stroke to ensure the TSV micromachining uniformity, which has become a big challenging issue for developing of high-end mask alignment positioning stages [1].

Generally, the common positioning stages can be divided into two categories: 1) ball screw-guided stages driven by servo motors, 2) linear guided stages driven by linear motors, in which there are some common defects including assembly gap, wear and aging, friction error and so on, which has restricted its further applications in the semiconductor manufacturing industries. In recent years, flexure-based nanopositioning stages driven by PZT actuator have been widely used in various micro/nano machining fields due to its outstanding advantages, e.g. high response speed, high precision, frictionless, and zero-backlash [2]. However, the common piezo nanopositioning stages have the problems of small travel range ($<$1mm), which makes them unsuitable for positioning targeted for millimeter scale tasks [3].

A number of preliminary studies have been conducted to solve this problem, the proposed solutions can be summarized as follows: 1) flexible mechanical displacement amplification [4]–[6]. Generally, lever displacement amplifier has been most widely employed due to its simple structure, however, the conventional lever displacement amplifier has a limited DAR resulting from the structure size constraint; 2) large-stroke motor actuation. In these actuators, voice coil motor(VCM) are most widely selected to drive the flexure-guided positioning stages due to its advantages of large stoke and fast response speed. Unfortunately, the VCM-driven positioning stage is difficult to realize nanopositioning, which is caused by the low resolution and low push force of the VCM actuator [7]. In addition, the problem of cross-talk defect in terms of input motion coupling and output motion coupling is also a big trouble, which should be suppressed to improve the stage positioning accuracy [8].

To cater for this requirement, this paper proposes a new type of XY nanopositioning stage based on the previous work. Two pairs of flexure-guided kinematic modules with large displacement amplification ratio are adopted to construct a 4-PP XY nanopositioning stage. A new decoupling design is to eliminate the cross-talk behavior between the input actuators and output compliant limbs, respectively. With consideration of repeatability property of TSV stage motion trajectory, as well as the decoupling property of the proposed nanopositioning stage, a repetitive-compensated PID (RCPID) controller

This work was supported in part by Natural Science Foundation of China(5160051494,U1601202,51675106,51575544), Science and Technology Program of Guangzhou(201510010058), Natural Science Foundation of Guangdong (2014A030310204), Guangdong General Programs for Science and Technology(2015A010104009,2015B010104008,2015B010133005).

H. Tang, J. Gao, X. Chen, Y. He, X. Chen, Z. Zeng, S. He, C. Chen are with Key Laboratory of Precision Microelectronic Manufacturing Technology & Equipment of Ministry of Education, Guangdong University of Technology, Guangzhou, China, and H. Tang is also with State Key Laboratory in Ultra-precision Machining Technology and Advanced Optics Manufacturing Centre, The Hong Kong Polytechnic University, Hong Kong SAR, China.

K. Yu, S. To and Y. Li are with Department of Industrial and Systems Engineering, The Hong Kong Polytechnic University, Hung Hom, Kowloon, Hong Kong SAR, China. *Corresponding authors: Chenx@gdut.edu.cn (Xin Chen);yangmin.li@polyu.edu.hk (Yangmin Li)

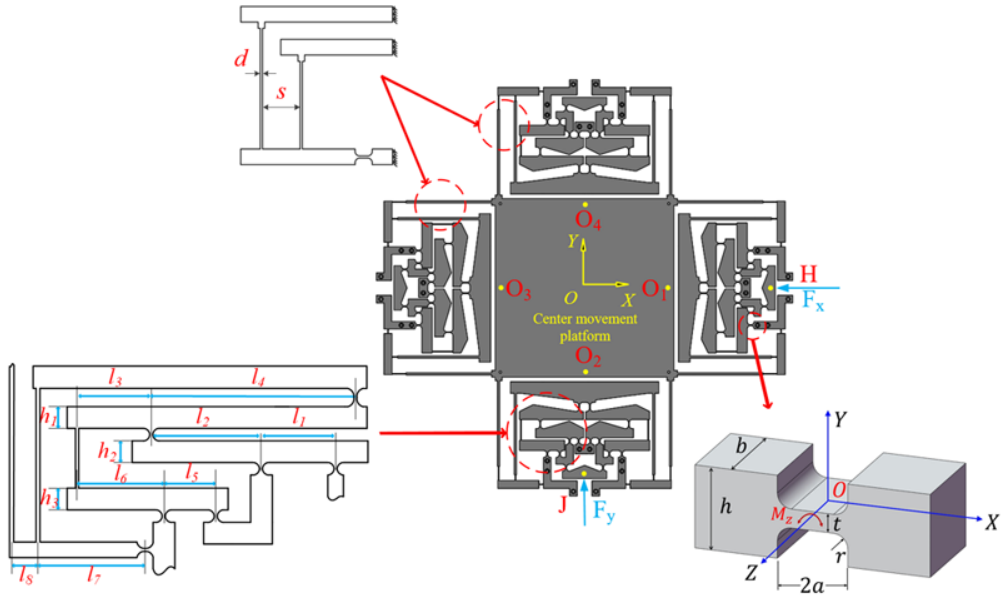

Fig. 1. The proposed XY nanopositioning stage.

and a SISO closed-loop control strategy are designed in this work, which aims to enhance the closed-loop positioning performance of the fabricated prototype. Finally, a series of closed-loop experimental tests are carried out in details. It indicates that the workspace of fabricated prototype has reached to 1.035mm×1.035mm, the cross-talk ratio is kept within 0.5%, and the closed-loop positioning accuracy is determined as 400nm. All the theoretical and experimental test results uniformly verify that the proposed nanopositioning stage has a satisfactory performance for fulfilling the TSV mask alignment task.

The major contribution of this work is the development, modeling, and controlling test of a completely decoupled nanopositioning stage with millimeter scale workspace and nanometer scale positioning accuracy. The organization structure of this paper is concluded as follows: firstly, the mechanism design and kinematics modeling are presented and discussed in Section II and Section III, respectively; then, dimension optimization via PSO algorithm is carried out in Section IV; thereafter, the mechanism performance evaluation via ANSYS Workbench is presented in Section V; furthermore, the closed-loop controller design, prototype test experiments, and the performance discusses are carried out in Section VI; finally, the study achievements are concluded in Section VII.

II. Nanopositioning Stage Design

The main purpose of this Section is to design a XY nanopositioning stage with millimeter scale workspace and nanometer scale positioning accuracy. As shown in Fig.1, flexure is adopted in this design due to its benefit such as compact structure, no mechanical friction, no assembly gap, and high response speed [9]. As for the actuator selection, PZT actuator is adopted, since comparing to the other actuators such as shape memory alloy (SMA), thermal, electrostatic actuators, and common linear motors, it possesses the advantages of ultra-large driving force, nanometer-scale motion resolution, and high response rate. However, the common PZT actuators have limited motion travel range($<200\mu$m), which greatly constraints theirs applications targeted millimeter motion range operations [10]. With these considerations, two pairs of flexure-guided kinematic modules with high displacement amplification ratio are adopted to construct a 2-PP XY nanopositioning stage. Flexible mobile deputy is adopted in this design, then an elaborate decoupling design is implemented aiming to completely eliminate the cross-talk behavior between the input actuators and output compliant limbs, respectively. In this kinematic module design, the corner-filleted flexure hinge is adopted since it has a superior property of both high motion precision and large travel range.

In this study, a 4-PP decoupled structure is built based on 2-PP parallel mechanism with orthogonal structure, and the double four-bar parallelogram flexures (FGKM) are adopted as the prismatic joints. The whole mechanism with mirror symmetry design is used to increase the stiffness and load-bearing characteristics of the center moving platform. In addition, symmetrical structure makes the whole mechanism more robust when confronts diverse manufacturing and assembly errors, and can reduce the effects of temperature gradient and environmental disturbance. The output part uses the void-cut way to reduce its unnecessary weight, which will totally improve the natural frequency of flexible nanopositioning stage. As for material selection of stage fabrication, we should make δ_y/E of the material as high as possible and its density as low as possible. With these considerations, AL7075-T6 workpiece is adopted to fabricate the prototype due to its satisfactory property [11], [12].

III. Kinematics Modeling

There are several methods for modeling the kinematics of flexure-guided compliant mechanism. In this section, a series of kinematics modeling in terms of output compliance, input stiffness, displacement amplification ratio modeling, and

workspace derivation are carried out via the compliance matrix method, since the factor-based compliance matrix computation can achieve higher efficiency and higher precision [13].

A. Output Compliance Modeling

As shown in Fig.1, according to the compliant mechanism theory, the relationship between the applied load and the output displacement can be described as follows,

$$\begin{bmatrix} \theta_1 \\ \Delta y_1 \\ \Delta x_1 \end{bmatrix} = \begin{bmatrix} C_{\theta,M_z} & C_{\theta,F_y} & 0 \\ C_{y,M_z} & C_{y,F_y} & 0 \\ 0 & 0 & C_{x,F_x} \end{bmatrix} \begin{bmatrix} M_{z1} \\ F_{y1} \\ F_{x1} \end{bmatrix} \quad (1)$$

where θ_1, Δy_1, and Δx_1 denote the flexure's rotational deformation, Y-axis deformation, and X-axis deformation, respectively, in the case of an external load M_{z1}, F_{y1}, and F_{x1} are applied on the three axes. The compliance factors C_i in the matrix have been presented in [14], [15]. In the coordinate O_i, compliance C_i can be converted into the coordinate O_j by using the following formula

$$\mathbf{C}_i^j = \mathbf{T}_i^j \mathbf{C}_i \left(\mathbf{T}_i^j\right)^T \quad (2)$$

where$\mathbf{T}_i^j$is the transformation matrix. It can be described as,

$$\mathbf{T}_i^j = \begin{bmatrix} \mathbf{R}_i^j & \mathbf{S}\left(r_i^j\right)\mathbf{R}_i^j \\ 0 & \mathbf{R}_i^j \end{bmatrix} \quad (3)$$

where $\mathbf{R}_i^j$ is the rotation matrix related coordinate O_i to the coordinate O_j. In series flexure, the output motion of the end-effector is accumulated by the deflection of the elastic deformation of whole flexure hinges, thus we can get the compliance $\mathbf{C}$ of series flexure through the following formula **X=CF**,

$$\mathbf{C}_O = \sum_{i=1}^{k} \mathbf{T}_{O_i}^O \mathbf{C}_{O_i} \left(\mathbf{T}_{O_i}^O\right)^T \quad (4)$$

where $\mathbf{C}$ denotes the accumulation of each flexure's compliance. In a parallel flexure, the high precision output motion of the end-effector is benefited from every parallel flexure. According to the formula **F=KX**, the stiffness of the parallel flexure can be expressed as an accumulation of each flexure' stiffness. As compliance is the reciprocal of stiffness, the compliance of a parallel mechanism can be expressed as:

$$\mathbf{C}_O = \left(\sum_{i=1}^{k} \left(\mathrm{T}_{O_i}^O \mathbf{C}_{O_i} \left(\mathbf{T}_{O_i}^O\right)^T\right)^{-1}\right)^{-1} \quad (5)$$

As the whole FGKM mechanism is a symmetrical structure, hence we analyze a quarter of the whole body firstly(see Fig.2). ${\mathbf{C}_B}^A$ is the compliance matrix of the output part B relative to the input part A.

$$\begin{aligned} \mathbf{C}_B^A &= \mathbf{T}_{14}^B(\mathbf{K}_I + \mathbf{K}_{II})^{-1}\left(\mathbf{T}_{14}^B\right)^T + \mathbf{T}_8^B \mathbf{C}_8 \left(\mathbf{T}_8^B\right)^T + \mathbf{T}_1^B \mathbf{C}_1 \left(\mathbf{T}_1^B\right)^T \\ &= \mathbf{T}_{14}^B \left[(\mathbf{C}_I)^{-1} + (\mathbf{C}_{II})^{-1}\right]^{-1} \left(\mathbf{T}_{14}^B\right)^T + \mathbf{T}_8^B \mathbf{C}_8 \left(\mathbf{T}_8^B\right)^T \\ &+ \mathbf{T}_1^B \mathbf{C}_1 \left(\mathbf{T}_1^B\right)^T \end{aligned} \quad (6)$$

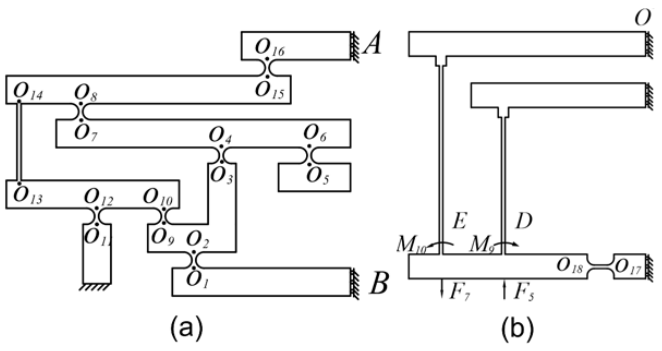

Fig. 2. The flexure-guided kinematic module (a) and flexure-guided parallel mechanism (b).

$$\mathbf{C}_I = \mathbf{T}_6^{14}\left\{\left[\mathbf{T}_3^6 \mathbf{C}_3 \left(\mathbf{T}_3^6\right)^T\right]^{-1} + \mathbf{C}_6^{-1}\right\}^{-1} \left(\mathbf{T}_6^{14}\right)^T + \mathbf{T}_7^{14} \mathbf{C}_7 \left(\mathbf{T}_7^{14}\right)^T \quad (7)$$

$$\mathbf{C}_{II} = \mathbf{T}_{12}^{14}\left\{\left[\mathbf{T}_{10}^{12} \mathbf{C}_{10} \left(\mathbf{T}_{10}^{12}\right)^T\right]^{-1} + \mathbf{C}_{12}^{-1}\right\}^{-1} \left(\mathbf{T}_{12}^{14}\right)^T + \mathbf{C}_{14} \quad (8)$$

$$\mathbf{C}_B = {\mathbf{K}_B}^{-1} = \left[({}_l\mathbf{C}_B)^{-1} + \left(\mathbf{T}_r^l\right)^{-T} ({}_l\mathbf{C}_B)^{-1} \left(\mathbf{T}_r^l\right)^{-1}\right]^{-1} \quad (9)$$

where $\mathbf{T}_j^i$ is the transformation matrix, ${}_l\mathbf{C}_B$ is the compliance matrix of the left half, ${}_r\mathbf{C}_B$ is the compliance matrix of the right half,

$${}_l\mathbf{C}_B = \mathbf{C}_B^A \quad (10)$$

$${}_r\mathbf{C}_B = \mathbf{T}_{rl}^l \mathbf{C}_B \left(\mathbf{T}_r^l\right)^T \quad (11)$$

$${}_l\mathbf{C}_P = \mathbf{T}_G^E \left[{\mathbf{C}_G}^{-1} + \left(\mathbf{T}_D^G\right)^{-1} (\mathbf{C}_D)^{-1} \left(\mathbf{T}_D^G\right)^{-T}\right]^{-1} \left(\mathbf{T}_G^E\right)^T + \mathbf{C}_E \quad (12)$$

$${}_r\mathbf{C}_P = \mathbf{T}_{rl}^l \mathbf{C}_P \left(\mathbf{T}_r^l\right)^T \quad (13)$$

$$\mathbf{C}_P = {\mathbf{K}_P}^{-1} = \left[({}_l\mathbf{C}_P)^{-1} + \left(\mathbf{T}_r^l\right)^{-T} ({}_l\mathbf{C}_P)^{-1} \left(\mathbf{T}_r^l\right)^{-1}\right]^{-1} \quad (14)$$

$$\mathbf{C}_{Limb_1} = \mathbf{C}_B + \mathbf{C}_P \quad (15)$$

$$\mathbf{C}_{out} = \left[(\mathbf{C}_{Limb_1})^{-1} + (\mathbf{C}_{Limb_2})^{-1} + (\mathbf{C}_{Limb_3})^{-1} + (\mathbf{C}_{Limb_4})^{-1}\right]^{-1} \quad (16)$$

The output compliance of the stage is just the compliance of the whole stage at the output platform center, which affects the bearing characteristics of the stage. That is, the smaller the output compliance, the higher the carrying capacity.

B. Input Stiffness Modeling

$\mathbf{C}_D$ denotes the compliance at the point D of the stage without the amplifier 1, the stiffness $\mathbf{k}_A^D$ is defined as the stiffness point A in the input part relative to the point D in the output part.

Based on the virtual work principle, we can get

$$F_i = \frac{\partial U}{\partial d_i} = 6K \left[\frac{1}{{L_1}^2} + \frac{1}{{L_2}^2} + \frac{1}{{L_3}^2}\left(\frac{L_6}{L_5} + \frac{L_1 + L_2}{L_1}\right)^2\right] d_i \quad (17)$$

where U denotes the kinetic energy of the stage. Then, the input stiffness of amplifier 1 can be expressed as follows,

$$\mathbf{K}_A^D=\frac{F_i}{d_i}=6\mathbf{K}\left[\frac{1}{{L_1}^2}+\frac{1}{{L_2}^2}+\frac{1}{{L_3}^2}\left(\frac{L_6}{L_5}+\frac{L_1+L_2}{L_1}\right)^2\right] \tag{18}$$

Therefore, the input stiffness is derived as,

$$\mathbf{K}_{in}=\left[\mathbf{C}_D+\left(\mathbf{K}_A^D\right)^{-1}\right]^{-1} \tag{19}$$

C. Displacement Amplification Ratio Modeling and Workspace Determination

In the process of flexure-guided positioning, every single flexure hinge would occur angular deformation, tensile and compressive deformation, which could make the flexure rotary offset from the center of the flexure, and affect the displacement amplification ratio and its workspace. Set the axial force acting on the flexure hinge as F_i, and the torque as M_i, axial deformation as Δ_i, rotation angle as α_i, so the relationship between deformation, force, and torque can be described as: $\Delta_i=\mathbf{F}_i\cdot\mathbf{C}_F$, $\alpha_i=\mathbf{M}_i\cdot\mathbf{C}_M$, where C_F is the axial compliance coefficient, C_M is the rotating compliance coefficient of the flexure hinge.

The schematic diagram of lever force model is shown in Fig.3(a-b), the flexure hinge at the fixed end can be seen as simplified version of the flexible pivot composed of spiral spring and linear spring, and the other flexure hinge can be seen as a simplification of the coil spring. The effect of θ_4 and θ_5 can be ignored since the orthogonal kinetic energy of the FGKM mechanism is quite small, which is due to its minimum cross-talk behavior.

As shown in Fig.3(c) and Fig.3(d), the output displacement of the FGKM mechanism can be expressed as a superposition of two parts: $d_o=d_4+d_8$, where d_4 and d_8 are the output displacement of the first and second lever, respectively.

$$d_4=\left(Y_8-\frac{Y_8Y_{10}Y_{11}}{1+Y_9Y_{10}}+\frac{Y_9Y_{11}}{1+Y_9Y_{10}}\frac{F_4}{d_1}\right)\left(Y_8+\frac{Y_9\left(1+Y_9Y_{10}\right)}{Y_9Y_{11}+Y_8d_1/F_4}\right)d_1 \tag{20}$$

$$d_8=-\frac{F_7Y_{14}}{l_6Y_{12}}+\frac{\left(l_6Y_{12}+l_4Y_{13}\right)\left(d_5l_6^2Y_{12}^2+d_5l_4l_6Y_{12}Y_{13}-F_7Y_{14}Y_{16}\right)}{l_6Y_{12}\left(l_6^2Y_{12}^2-Y_{14}Y_{15}\right)} \tag{21}$$

Finally, the DAR value($A=\frac{d_o}{d_{in}}=\frac{d_4+d_8}{d_1}$)of the FGKM mechanism can be derived:

$$\begin{aligned}A=&\left(Y_{I_18}-\frac{Y_{I_18}Y_{I_111}Y_{I_210}}{1+Y_{I_19}Y_{I_210}}+\frac{Y_{I_19}Y_{I_211}}{1+Y_{I_19}Y_{I_210}}\frac{F_{I_2o}}{d_1}\right)\left(Y_{I_28}\right.\\&\left.+\frac{Y_{I_29}\left(1+Y_{I_19}Y_{I_210}\right)}{Y_{I_19}Y_{I_211}+Y_{I_18}d_1/F_{I_2o}}\right)-\frac{F_{II_2}Y_{14}}{L_6Y_{12}d_1}+\\&\frac{\left(L_6Y_{12}+L_4Y_{13}\right)\left(L_5L_6{}^2Y_{12}{}^2+L_5L_4L_6Y_{12}Y_{13}-F_{II_2}Y_{14}Y_{16}\right)}{L_6Y_{12}\left(L_6{}^2Y_{12}{}^2-Y_{14}Y_{15}\right)}\end{aligned} \tag{22}$$

where Y_i denotes the computation factor, here let T denotes the actual maximum steady-state output displacement of the PZT actuator, the workspace of the nanopositioning stage can be determined as $AT\times AT$ if the material failure is successfully avoided. In the next section, the dimension optimization tasks will be fulfilled to maximize the displacement amplification ratio and workspace.

IV. Dimension Optimization via PSO Algorithm

As mentioned above, a high DAR value(A)is required, while it will reduce the stiffness k_{in} of a compliant mechanism. Moreover, a compact positioning stage is desirable for the practical TSV lithography micromachining applications, where the mask alignment operations are conducted in a limited space, a series of size constraints should be satisfied to ensure the monolithic flexure positioning stage has a compact structure.

A. Optimization Statement

In Fig.1, the main dimension parameters of flexure are: r, t, b, the parameters of lever displacement amplifier: L_1, L_2, L_3, L_4, L_5, L_6, H_1, H_2, H_3, the dimension parameters of straight beam flexure: L_7, L_8, d, s, the overall thickness of the stage w. In order to get a high natural frequency, we specify H_1=7mm, H_2=8mm, H_3=9mm. In order to ensure that beam flexure rigid enough, we specify d=2mm, s=15mm; in order to ensure the amplifiers with compact structure, we select L_1=8mm, L_5=11mm, L_6=23mm, L_7=22.5mm, L_8=14.5mm.

This optimization problem can be described as follows:

1) Objective: maximize A
2) The parameters need to optimize: r, t, L_2, L_3, L_4
3) Constraints:
   a)corner-filleted flexure parameter: $0.05\leq t/r\leq 0.65$
   b)the stiffness relationship: $k_{in}\leq k_p$
   c)stress constraint: $\max\{\sigma_r,\ \sigma_t\}\leq\ \sigma_y/\text{sf}=\sigma_a$
   d)size range: 2.5mm$\leq r\leq$5mm,0.5mm$\leq t\leq$2mm,20mm$\leq L_2\leq$30mm,10mm$\leq L_3\leq$20mm,30mm$\leq L_4\leq$40mm,$L_3+L_4\leq$55mm.

The dimension optimization(t/r) of corner-filleted flexure hinge is conducted to ensure the compliance matrix factor C_i has a high precision. The dimension optimization of $k_{in}\leq k_p$ aims to reduce the PZT actuator's input displacement loss at the driving point. To avoid the stage occurring failure in the stress phase, $\max\{\sigma_r,\sigma_t\}\leq\sigma_y/\text{sf}$ should be ensured with a safety factor sf=2. Besides, the thinnest part of the corner-filleted flexures is no less than 0.5mm since the designed nanopositioning stage will be fabricated by using the wire-electro-discharge-machining (WEDM) technique which cannot ensure a tolerance of $\pm$0.01mm once the machining material thickness is smaller than 0.5mm.

B. Optimization Results

The optimization work is carried out by using the MATLAB PSO toolbox with the penalty function method [16]. After a series of iterations, the final optimized mechanism parameters are: r=2.8mm, t=0.8mm, L_2=25.7mm, L_3=17mm, L_4=34.2mm, A=12.3.

V. FEA Analysis and Evaluation

In this section, the stage performance is evaluated by the ANSYS Workbench. A new project is established with the new material parameters of E(Young's modulus)=71.7GPa, σ(yield strength)=503MPa, υ(Possion

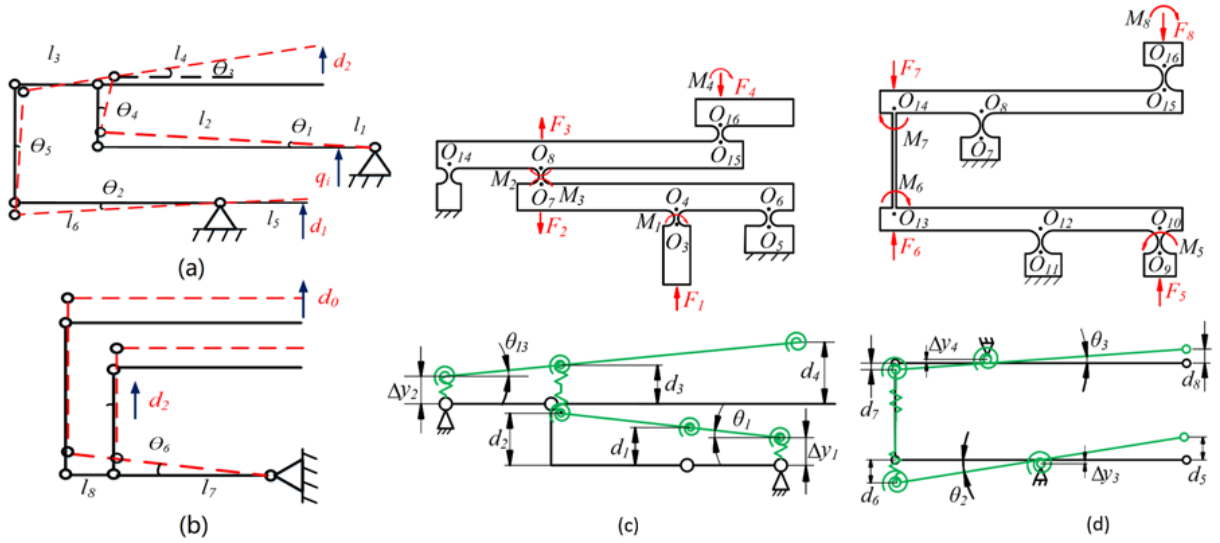

Fig. 3. The schematic diagram of the total lever force model(a-b), the first (c) and the second (d) lever force model.

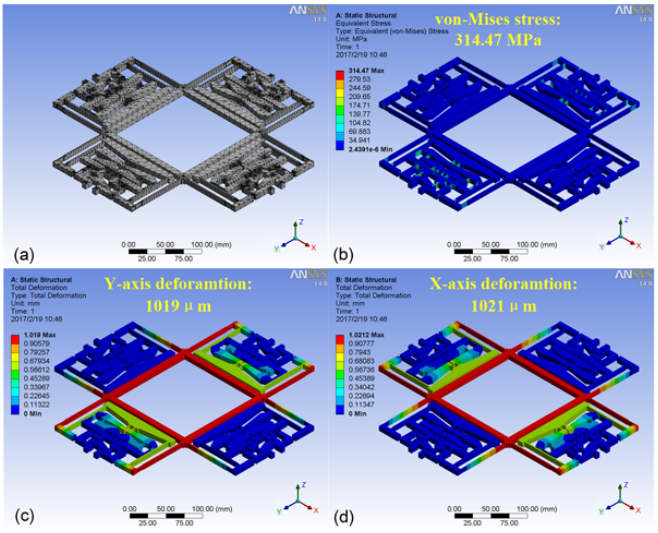

Fig. 4. FEA static structural analysis results.(a)3D FEA model, (b)Von-Mises stress analysis result, (c)Y-axis deformation, (d)X-axis deformation

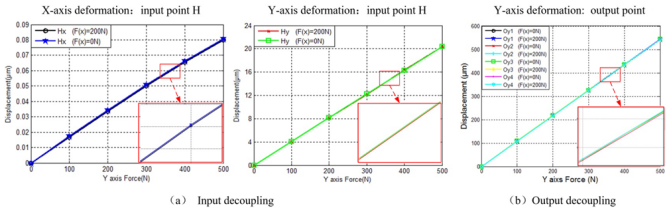

Fig. 5. FEA analysis results of cross-talk. (a)Input decoupling analysis result, (b)Output decoupling analysis result.

rate)=0.33, ρ(density)=2810Kg/m^3. A 3D finite element model is built up with software Solidworks(Fig.4(a)). The static structural and modal analysis processes are described as follows.

A. Static Structural Analysis

1) Exerting Driving Force in X Axis : In order to validate the amplification and the decoupling property of the optimized stage, we exert driving force on the point H, the deformation relation and the property evaluation in the following points are: the ratio of d_{yo1}, d_{yo2}, d_{yo3}, d_{yo4}, and d_{yH} denote the relationship between the workspace of stage and the output displacement of actuator, d_{xo1}, d_{xo2}, d_{xo3}, d_{xo4} denote the output point's parasitic movement; d_{xJ} denotes the displacement in the X direction output point, error1=max$\{d_{xoi}/d_{yoi}\}$ denotes the maximum output coupling error, error2=max$\{d_{xJ}$, $d_{yJ}\}/d_{yoi}$ denotes the maximum input coupling error.

When exerting 1000N force on the point H, the Von Mise stress, the X-axis deformation, and the Y-axis deformation are displayed in Fig.4(b-d), respectively. It can be seen that it has a very small effect on the whole stage deformation when occurring deformation in X axis, which verifies that the Y direction displacement has not been affected by the X direction displacement. In order to evaluate the accuracy, then we exert a set of forces [100, 200, 300, 400, 500] on the point H of the Y direction (Table I). It indicates that: with driving force increasing, all displacements of the key points increase under a constant ratio, which validates that there is a linear relationship between input force and output displacement of the stage. When applying a driving force on the point H in y direction, the maximum deformation at the output part of the stage takes place on O_2, O_4, and the coupling error is 0.07%, the maximum coupling error of O_1 and O_3 is only 0.03%. Possible causes for the discrepancy are the elastic deformation of the rigid body and stage assembly errors. The input coupling maximum error is only 0.0002%; the displacement amplifier ratio A of the stage is 12.1.

2) Exerting Force in X and Y Direction at the Same Time: In order to meet the practical demand, we need to exert the driving force on the point H and J at the same time. Because the structure is symmetric, we simply verify the influence by comparing the change of displacement(d_{xH},d_{yH})at H point

TABLE I
THE STATIC STRUCTURAL ANALYSIS DATA

Parameters	100N	200N	300N	400N	500N
$d_{xH}(\mu m)$	0.02	0.03	0.05	0.07	0.08
$d_{xJ}(\mu m)$	-2.05E-04	-4.20E-04	-6.34E-04	-8.55E-04	-1.05E-03
$d_{yH}(\mu m)$	8.08	17.35	26.22	35.31	43.36
$d_{yJ}(\mu m)$	2.93E-05	6.12E-05	9.20E-05	1.17E-04	1.43E-04
$d_{xO1}(\mu m)$	0.03	0.08	0.08	0.11	0.16
$d_{xO2}(\mu m)$	0.06	0.12	0.16	0.25	0.37
$d_{xO3}(\mu m)$	-0.03	-0.07	-0.07	-0.09	-0.15
$d_{xO4}(\mu m)$	-0.06	-0.13	-0.15	-0.25	-0.36
$d_{yO1}(\mu m)$	102.61	209.94	317.26	426.25	524.66
$d_{yO2}(\mu m)$	102.58	209.91	317.24	427.22	524.61
$d_{yO3}(\mu m)$	102.61	209.92	317.26	427.23	524.63
$d_{yO4}(\mu m)$	102.60	209.90	317.25	427.21	524.60
Error1	0.06%	0.07%	0.05%	0.06%	0.07%
Error2	0.0002%	0.0002%	0.0002%	0.0002%	0.0002%
A	12.1	12.1	12.1	12.1	12.1

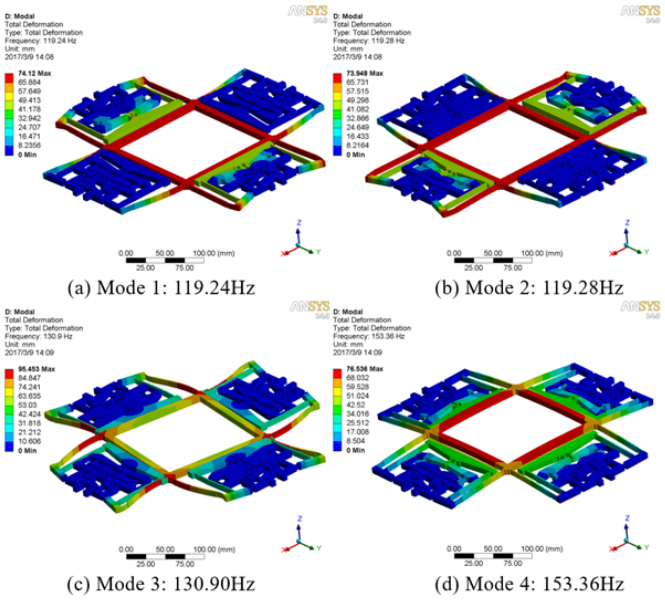

Fig. 6. Modal analysis results.

in the X direction under the driving force and the output displacement of the stage along the Y axis. According to the Fig.5(a), it indicates that branched-chain driving force on the Y axis has a small displacement effect on the displacement of the output part, and the displacement error is only 0.004μm, input coupling error is only 0.0002%. According to Fig.5(b), we can know that branched-chain driving force on the X axis has a small displacement effect on the displacement of the output part, then, the displacement error is determined as 0.1μm, and the input coupling error is determined as 0.06%. As shown in Table I, all the FEA simulation results indicate that the stage has a decoupling property in terms of input and output motion.

B. Modal Analysis

As shown in Fig.6, the deformation of mode 1-2 occur along x axis and y axis, respectively. As the completely symmetric

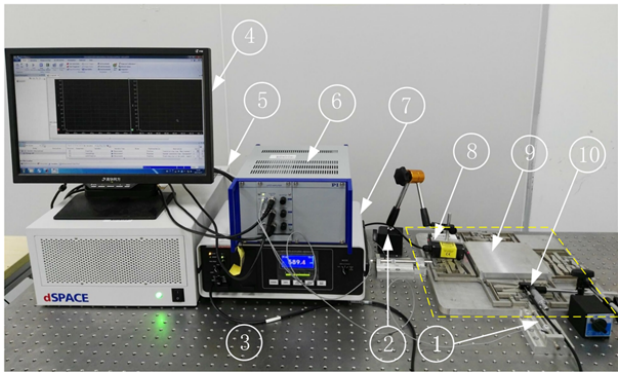

Fig. 7. Experimental setup. 1) PZT actuator, 2) Magnetic gauge stand, 3) Vibration isolation stage, 4) Host controlling computer, 5) dSPACE control system, 6) Voltage amplifier, 7) Fiber-optic displacement sensor, 8) Laser displacement sensor, 9) Nanopositioning stage, 10) Fiber-optic displacement sensor probe.

structure, the deformation of the nanopositioning stage in the x and y axis are quite consistent, and the resonance frequencies are quite close (119.24Hz and 119.28Hz). The mode 3 and 4 are rotational deformation and shear deformation, respectively. Its resonance frequencies are 130.90Hz and 153.36Hz. Obviously, the XY nanopositioning stage is mainly work under the applying forces and generate deformation in XY direction, respectively. Therefore, the first two natural frequencies of the stage are critical for the overall positioning performance. The theoretical calculations and dimension optimization carried out in Section III-IV has improved the first two frequencies, which can be used to enhance the mask aligning efficiency of the TSV laser lithography system.

VI. CONTROLLER DESIGN AND EXPERIMENTAL TESTS

In this Section, the optimized nanopositioning stage is fabricated. To evaluate the performance of the prototype, a novel RCPID controller is proposed. Then, a series of experimental tests in terms of open-loop measurement, cross-talk test, dynamic hysteresis nonlinearity characterization, and closed-loop sinal trajectory tracking tests are carried out in detail.

A. Experimental Setup

A piece of AL7075-T651 material is adopted to fabricate the experimental prototype via the WEDM (wire electro-discharge machining) method. The whole experimental system is displayed in Fig.7. Two PZT actuators (P-840.60, PI) with a 3-channel voltage amplifier (E-503,PI) are used to actuate the nanopositioning stage. The laser displacement sensor (LTS-025-04, MTI) and fiber-optic displacement sensor (MTI-2100, MTI) are utilized to measure the precision displacement of the stage. The closed-loop control of this stage is achieved by using the dSPACE rapid prototyping simulating system (DS-1007,dSPACE). In order to avoid the external vibration from all kinds of disturbances, all instruments (except the PC) are placed on the vibration isolation stage (WN01AL, Winner optics).

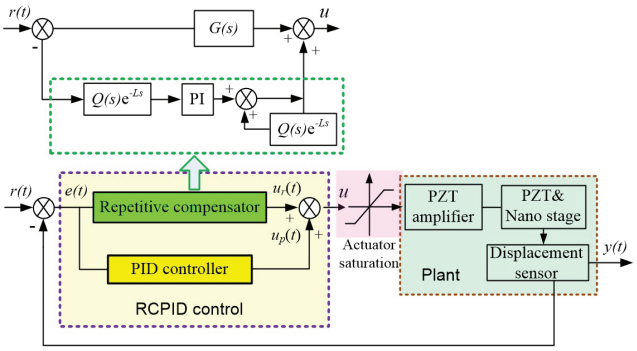

Fig. 8. The designed repetitive-compensated PID controller.

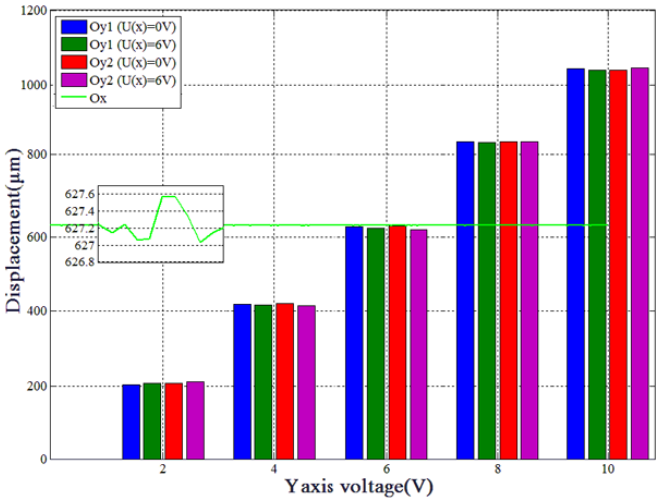

Fig. 9. Cross-talk test results.

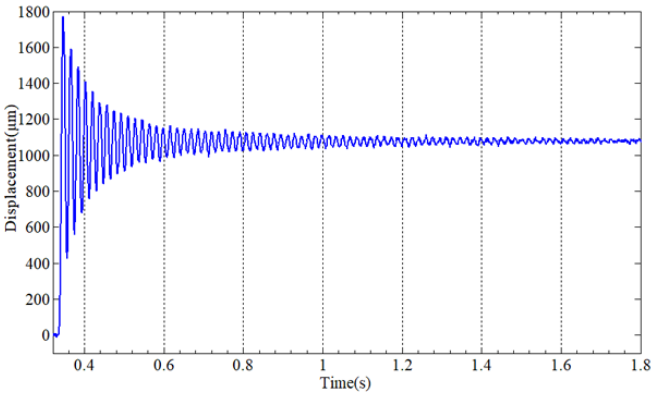

Fig. 10. The free vibration damping curve.

B. SISO Closed-loop Control Strategy Design

With consideration of repeatability property of TSV mask alignment system, the driving signal is obvious regular and repeatable, thus, repetitive controlling strategy is employed in this test. With the consideration of the stability problem of the repetitive controller, the traditional PID controller is still employed in this control. As shown in Fig.8, a novel RCPID controller is proposed in this paper. It is composed of a PID control unit and a repetitive compensating unit [17], where $r(t)$ denotes the planned command signal, $e(t)$denotes the error signal, $u_r(t)$ denotes the control signal generated by the repetitive compensator, $u_p(t)$ denotes the control signal generated by the PID controller, $Q(s)e^{-Ls}$ denotes the sampling signal low-pass filter and delay unit, PI denotes the Proportion Integration control unit. With consideration of the post-error of the nanopositioning stage, the two control signals are combined to drive the PZT actuators and the flexure-based nanopositioning stage to output a precision motion. Besides, this closed-loop control strategy is designed to run in a SISO (Single-input-single-output) manner due to the stage's totally decoupling property [18]. Moreover, a LMS filter is added to this block diagram in order to eliminate the disturbances arising from circuit noises and environmental noises.

C. Experimental Implementation

1) Open-loop Test: First, a few groups of open-loop experiments have been carried out. A set of voltages (0-10V) is applied to the Y-axis PZT and X-axis PZT in sequence. By acquiring the output displacement at the point O_1, O_2 with the fixed sampling step. Then we applied a 6V constant voltage on X axis PZT while applied a set of voltages (0-10V) on the Y axis PZT. Two groups of experimental results are recorded and displayed in Fig.9. It can be observed that the X axis drive input displacement has little influence on the Y axis drive output displacement(displacement deviation: 0.81μm, output coupling error: 0.5%).

In order to further validate the performance of the stage, first, the free vibration damping curve is obtained via exerting a step signal(10V) to drive the stage. As shown in Fig.10, the interval period between two peaks is around 0.009s, that is the vibration frequency of the mechanism is 109.4Hz, the angular frequency is 690.5rad/s, and the damping ratio is determined as 0.013. It indicates that the resonance frequency of the mechanism is close to the FEA simulation result (119Hz). Second, hysteresis nonlinearity characterization is conducted. By applying a set of sinusoidal signals with varying frequencies (0.25≤f≤10HZ) to the PZT actuators, the experimental data in terms of the output displacement and the driving voltage are recorded and plotted in Fig. 11 (with an interval of 0.0001s), it can be seen that the hysteresis loop is obvious rate-dependent, the higher the driving frequency, the wider the hysteresis loop (the worse the hysteresis nonlinearity). Therefore, a series of closed-loop positioning controls should be carried out to greatly improve the performance of this nanopositioning stage.

2) Closed-loop Test: In this Section, the motion tracking experiments are implemented to validate the designed RCPID controller and the performance of the developed nanopositioning stage. The established MATLAB/Simulink model is compiled and downloaded to the dSPACE system. The fixed-step size (fundamental sample time) is set to 0.001s, and the controller parameters are assigned as follows: K_p=0.02, k_i=45, k_d=0.00001(PID controller); K_p=0.8, k_i=1.2 (repetitive-compensator). During each sampling interval, the output displacement signal acquired by the fiber-optic displacement sensor is processed to generate the actual control voltage to drive the nanopositioning stage.

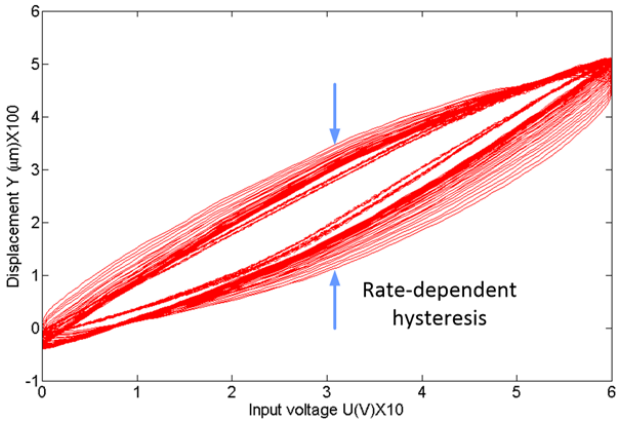

Fig. 11. Open-loop rate-dependent hysteresis nonlinearity curves with varying voltage frequencies.

TABLE II
THE PERFORMANCE COMPARISONS OF THE NANOPOSITIONING STAGES

Ref	Dimension (mm^2)	DAR	Bandwidth (Hz)	Workspace μm^2	Area efficiency
[9]	92×50	12.1	205	214μm	0.05
[11]	98×56	12.84	83	963μm	0.18
[12]	100×100	1	2k	15×15	0.02
[14]	220×220	1	719.49	19.2×18.8	0.01
[15]	250×250	5.85	115.6	117×117	0.22
This work	285×285	11.5	119.6	1035×1035	13.19

First, the common signal trajectory tracking control experiments are implemented. With a sinusoidal signal (ω=1.07 rad/s) applied to the X-axis PZT, the driving signal and the output displacement signal are recorded and plotted in Fig.12(a). It indicates that a high-precision trajectory tracking is achieved, the maximum peak-to-peak steady error is kept within the range of $\pm 0.2\mu$m, therefore, the closed-loop positioning accuracy is determined as 400nm; With a sawtooth wave signal(v=120μm/s) applied to the Y-axis PZT, as shown in Fig.12(b), the maximum peak-to-peak steady error and the closed-loop positioning accuracy is identical to the previous result, as well as the DAR value is determined as around 11.5(1035/90=11.5), thus the workspace reaches up to 1.035mm×1.035mm. As shown in Fig.13, there is a small derivation among workspaces from different calculations, which is resulting from the difference of the experimental conditions, machining error, and assembly error, etc.

It reveals that the error amplitude obviously decreases with time and finally becomes stable after several periods, which validates the stability of the controlled system. In order to further validate the stability of the positioning system, the open-loop and closed-loop Bode diagrams are plotted and displayed. Fig.14 indicates that the resonance frequency of the controlling system is 690.5rad/s(109.4Hz), which is close to the FEA result (119Hz), our ideal vibration frequency. According to the Bode stability criterion, the stability of the control system is verified.

D. Performance Evaluation and Discussion

When assessing a flexure-based nanopositioning stage, the positioning accuracy, travel range, resonance frequency, and

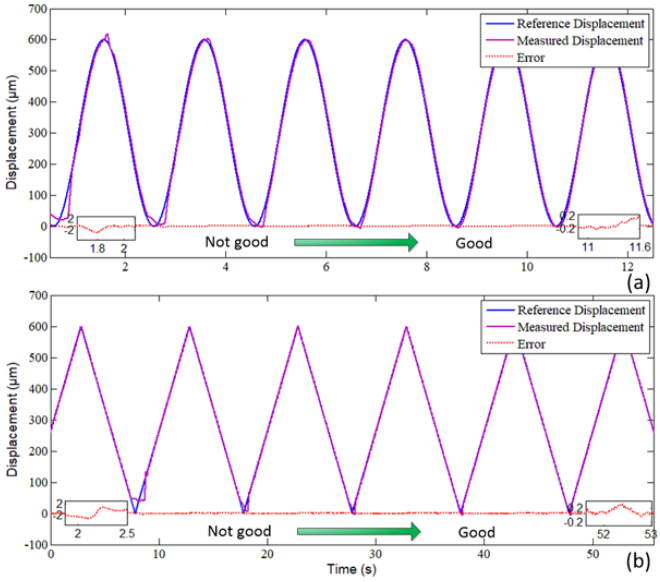

Fig. 12. The common signal trajectory tracking control results. a) with sinusoidal signal, ω=1.07 rad/s; b) with sawtooth signal, v=120μm/s.

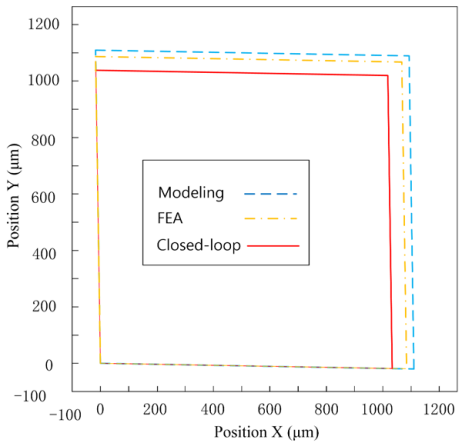

Fig. 13. The comparisons of the determined workspace with different methods.

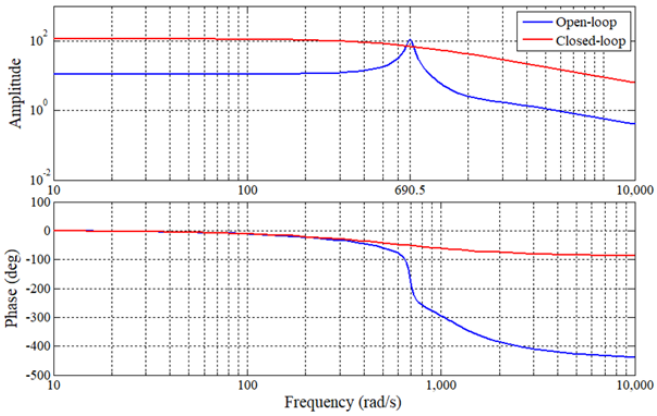

Fig. 14. The Bode diagram.

stage size should be totally considered since all of these performance parameters are coupled each other, it is difficult to directly compare one stage with other stage [11]. In order to objectively evaluate the performance of the tested stage, a concept of "area efficiency" (workspace/mechanism area) can be found in [8]. That is, the higher the area efficiency, the more effective of the nanopositioning stage, since it has a more compact structure. For a clearly comparison with the proposed flexure-guided XY nanopositioning stages, several typical mechanisms are listed in Table II. As shown in this table, the area efficiency value of the proposed stage is much higher than the other stages, which verifies that it has more satisfactory performance to be scaled down to realize TSV laser lithography mask alignment task.

VII. Conclusions

A flexure-guided XY positioning stage with millimeter scale workspace, decoupling property, and nanometer scale accuracy is developed in this work. The compliance matrix method is employed for the kinematic modeling and analysis in terms of output compliance, input stiffness, displacement amplification ratio modeling, and workspace derivation. A series of dimension optimization tasks are fulfilled via PSO Algorithm, which has improved the workspace of the nanopositioning stage. The model validation and performance evaluation of the optimized stage are fulfilled by the FEA method. In order to suppress the residual circuit noises, rate-dependent hysteresis nonlinearity, creep effect, assembly errors, and other unknown disturbances, a RCPID controller and a SISO closed-loop control strategy are designed. Finally, a series of experimental tests in terms of open-loop measurement and closed-loop tests are carried out in details. It indicates that the workspace of the fabricated prototype has reached to 1.035mm$\times$1.035mm, the cross-talk ratio is kept within 0.5%, and the closed-loop positioning accuracy is determined as 400nm.

References

[1] R. Abbaspour, D.K. Brown, and M.S. Bakir, "Fabrication and electrical characterization of sub-micron diameter through-silicon via for heterogeneous three-dimensional integrated circuits,"*J. Micromech. Microeng.*, vol. 27, pp. 025011, 2017.

[2] H. Kim, J. Kim,"Development of a nanoprecision 3-DOF vertical positioning system with a flexure hinge," *IEEE Trans. Nanotech.*, vol. 12, no. 2, March 2013.

[3] Xiantao Sun, Weihai Chen, et.al, "A decoupled 2-DOF flexure-based micropositioning stage with large travel ranges, "*Robotica*, vol.32, pp. 677-694, 2014.

[4] Y. Tian, B. Shirinzadeh, D. Zhang, and G. Alici, "Development and dynamic modelling of a flexure-based Scott-Russell mechanism for nanomanipulation,"*Mechan. Sys. Sig. Proc.*, vol. 23, pp. 957-978, 2009.

[5] P. R. Ouyang, W. J. Zhang, and M. M. Gupta, "Design of a new compliant mechanical amplifier," in *Proc. of ASME Int. Desi. Eng. Tech. Conf. & Comp. and Info. in Engi. Conf.*, Sept. 24-28, 2012, Long Beach, California, USA, pp. 1-10.

[6] M. -Y. Chen, H.-H. Huang, and S.-K. Hung, "A new design of a submicropositioner utilizing electromagnetic actuators and flexure mechanism," *IEEE Trans. Ind. Electron.*, vol. 57, no. 1, pp. 96-106, Jan. 2010.

[7] J. Shang, Y. Tian, Z. Li, et.al, "A novel voice coil motor-driven compliant micropositioning stage based on flexure mechanism,"*Rev. of Sci. Instru.*, vol. 86, pp. 095001-1-095001-10, 2015.

[8] H. Tang and Y. Li, "A new flexure-based Yθ nanomanipulator with nanometer scale positioning resolution and millimeter range workspace," *IEEE/ASME Trans. Mechatron.*, vol. 20, no. 3, pp. 1320-1330, June 2015.

[9] X. Zhu, X. Xu, Z. Wen, "A novel flexure-based vertical nanopositioning stage with large travel range," *Rev. of Sci. Instru.*, vol. 86, pp. 105112, 2015.

[10] F. Wang, C. Liang, Y. Tian, "A flexure-based kinematically decoupled micropositioning stage with a centimeter range dedicated to micro/nano manufacturing," *IEEE/ASME Trans. Mechatron.*, vol. 21, no. 2, April 2016.

[11] J.-J. Kim, Y.-M. Choi, "A millimeter-range flexure-based nanopositioning stage using a self-guided displacement amplification mechanism,"*Mechanism and Machine Theory*, vol. 50, pp. 109-120, 2012.

[12] S. Polit and J. Dong, "Development of a high-bandwidth *XY* nanopositioning stage for high-rate micro-nanomanufacturing," *IEEE/ASME Trans. Mechatron.*, vol. 16, no. 4, pp. 724-733, 2011.

[13] H. Tang and Y. Li, "Design, analysis and test of a novel 2-DOF nanopositioning system driven by dual-mode," *IEEE Trans. Robot.*, vol. 29, no. 3, pp. 650-662, June 2013.

[14] Y. Li, J. Huang, and H. Tang, "A compliant parallel XY micro-motion stage with complete kinematic decoupling," *IEEE Trans. Auto. Sci. Eng.*, vol. 9, no. 3, pp. 538-553, July 2012.

[15] H. Tang and Y. Li, "Feedforward nonlinear PID control of a novel nanomanipulator using Preisach hysteresis compensator," *Robotics and Computer-Integrated Manufacturing*, vol. 34, pp. 124-132, 2015.

[16] F. Tao, D. Zhao, Y. Hu, Z. Zhou, "Resource service composition and its optimal-selection based on particle swarm optimization in manufacturing grid system," *IEEE Trans. Ind. Inform.*, vol.4, no.4, pp. 315-327, Nov. 2008.

[17] Jinhua She, Lan Zhou, et.al,"Design of a modified repetitive-control system based on a continuous-discrete 2D model," *Automatica*, vol. 48, pp. 844-850, 2012.

[18] H. Tang and Y. Li, "Development and active disturbance rejection control of a compliant micro/nano positioning piezo-stage with dual-mode,"*IEEE Trans. Ind. Electron.*, vol. 61, no. 3, pp. 1475-1492, March 2014.

Hui Tang received the B.S. and M.S. degrees in automation and control from Jiangxi University of Science and Technology, Ganzhou, China, in 2005 and 2008, respectively, and the Ph.D degree in electromechanical engineering from the University of Macau, Macao, China, in 2014. From 2016 to 2018, he was a Postdoctoral Researcher with the Columbia University in New York and The Hong Kong Polytechnic University. He is currently an Associate Professor with the School of Electromechanical Engineering, Guangdong University of Technology, Guangzhou, China. He has published 40 academic papers in journals and conferences.

His interests include flexure mechanism and nanopositioning stages, semiconductor manufacturing equipment, micro/nano device manufacturing.

Jian Gao received her M.S. degree in mechanical engineering from Huazhong University of Science and Technology, China, in 1993 and her Ph.D degree in materials, mechanical and manufacturing engineering from the University of Nottingham, the UK, in 2002. From 2002 to 2004, she was a Post-doctoral Research Fellow with the School of Materials, Mechanical and Manufacturing Engineering, University of Nottingham, UK. She is currently a Professor with the School of Electromechanical Engineering, Guangdong University of Technology, Guangzhou, China.

Her research interests include semiconductor packaging equipment technology, digital manufacturing and remanufacturing engineering.

Xin Chen was born in Hunan, China, in 1960. He received his Ph.D. degree in mechanical engineering from Huazhong University of Science and Technology, China, in 1995. He is currently a Professor with the School of Electromechanical Engineering, Guangdong University of Technology, Guangzhou, China.

His research interests include mechanical dynamics, IC packaging equipment technology and precision machining and measurement.

Kai-Ming Yu obtained his B.S. & Ph.D. degrees from the Department of Mechanical Engineering, University of Hong Kong in 1985 and 1990, respectively, was a Postdoctoral Fellow in Hong Kong University of Science & Technology before joining PolyU as Lecturer in 1993 to teach various subdegree, degree, and postgraduate subjects. He is currently an Associate Professor of the Department of Industrial and Systems Engineering of The Hong Kong Polytechnic University.

His research interests include rapid product technologies, CAD/CAE/CAM, geometric modelling, and design innovation.

Suet To obtained her MPhil in Material Science from Brunel University in the UK in 1993, and her PhD in Ultra-precision Machining Technology from The Hong Kong Polytechnic University, HK SAR, China, in 2000. She is currently an Associate Professor of the Department of Industrial and Systems Engineering of The Hong Kong Polytechnic University and Associate Director of State Key Laboratory in Ultra-precision Machining Technology and Advanced Optics Manufacturing Centre.

Her research interests include ultra-precision machining, advanced optics manufacturing, and material science.

Yunbo He received the Ph.D. degree in mechatronics engineering from Xi'an Jiaotong University, Xi'an, China, in 2000. He was a Postdoctoral Fellow with Nanyang Technological University, Singapore, the Technical Manager with ASM Technology, Singapore, and the General Manager with Hans Photoelectric Equipment Co. Ltd. He is currently a Professor with the School of Electromechanical Engineering, Guangdong University of Technology, Guangzhou, China.

His research interests include motion control, high-precision electronic equipment, automation, and robotics.

Xun Chen was born in Hunan, China, 1988. He received his B.Eng in communication system engineering at University of Birmingham (UK), in 2010, and received his Ph.D. degree in system engineering at Brunel University West London (UK), in 2016. He is currently a Lecturer in school of Electromechanical Engineering at Guangdong University of Technology, Guangzhou, China.

His research areas include smart manufacturing, precision manufacturing, sustainable manufacturing systems, and machining tool designs.

Zhaohe Zeng received the B.S. degree in mechanical engineering and automation from Jiangxi University of Science and Technology, Ganzhou, China, in 2010 and 2014, respectively, and the M.S. degree in mechanical engineering from Guangdong University of Technology, Guangzhou, China.

His research interests include design of flexible microposioning stage and control of piezoelectric actuator.

Sifeng He was born in Sichuang, China, in 1997. He is currently working towards the B.S. degree in mechanical engineering in Guangdong University of Technology, Guangzhou, China.

His research interests include design of flexible micropositioning stage and control of piezoelectric actuator.

Chuangbin Chen was born in Guangdong, China, in 1995. He is currently working towards the B.S. degree in mechanical engineering in Guangdong University of Technology, Guangzhou, China.

His research interests include computer vision and control of robot.

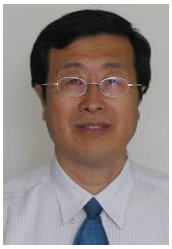

Yangmin Li (M'98-SM'04) received the B.S. and M.S. degrees from Jilin University, Changchun, China, in 1985 and 1988, respectively, and the Ph.D. degree from Tianjin University, Tianjin, China, in 1994, all in mechanical engineering. He is currently a Full Professor of the Department of Industrial and Systems Engineering of The Hong Kong Polytechnic University. He has authored and coauthored 381 scientific papers in journals and conferences.

His research interests include micro/nanomanipulation, compliant mechanism, precision engineering, robotics, multibody dynamics and control. Dr. Li is a Member of the ASME and CSME. He is an Associate Editor of the IEEE Trans. Auto. Sci. Eng., Associate Editor of Mechatronics, Associate Editor of the International Journal of Control, Automation, and Systems.